

# First-principles study of $\text{Ca}^{2+}$ and $\text{Mn}^{2+}$ substituents in $\text{KTaO}_3$

Kevin Leung

Sandia National Laboratories, Mail Stop 1421, Albuquerque, New Mexico 87185

(Received 25 April 2000; published 6 March 2001)

The structural properties, energetics, and dynamics of  $\text{Ca}^{2+}$  and  $\text{Mn}^{2+}$  substituents in  $\text{KTaO}_3$  are investigated from first principles. It is found that Ca substitutes for both K and Ta ions. Oxygen vacancies bind to isolated Ca ions residing at Ta sites, causing off-center Ca displacement and forming large dipoles. There is also evidence that oppositely charged defects may cluster together. Our calculations predict that the activation energy for dipole reorientation via oxygen vacancy hopping within the first-neighbor shell of Ta-substituting Ca or Mn exceeds 2 eV. On the other hand,  $\text{Mn}^{2+}$  substituting at the K site displaces off center along the (100) direction, also forming a dipole. This dipole can reorient via Mn hopping motion with an activation energy of  $\sim 0.18$  eV, in reasonable agreement with experiments. We argue that, in general, metal ion hopping at the A site, not oxygen vacancy hopping, is responsible for the small activation energies found in experiments.

DOI: 10.1103/PhysRevB.63.134415

PACS number(s): 77.84.Dy, 61.72.Ji

## I. INTRODUCTION

Impurity dipoles in ferroelectrics are vital to understanding relaxor behavior,<sup>1</sup> polarization pinning,<sup>2,3</sup> and fatigue in ferroelectric devices.<sup>4</sup> When a metal substituent resides off center at the A or B site of the perovskite ( $\text{ABO}_3$ ) structure—particularly if it binds to an oxygen vacancy in its first-neighbor shell—a dipole is created. This impurity dipole can usually orient in several equivalent, symmetry-related directions. When the host ferroelectric is near its critical point, the correlation length is large, and the interaction between even small concentration of impurity dipoles is propagated a large distance. As a result, ferroelectric behavior can be strongly affected, and glassy or relaxor behavior may result due to frustration of the dipolar interactions.<sup>5</sup> Likewise, during polarization switching via application of an external electric field to a ferroelectric, impurity dipoles are initially misaligned with respect to the field, and they pin the lattice in their neighborhood. An activation energy is required to realign them. As a result, polarization switching kinetics in ferroelectrics are strongly affected by impurity dipoles.<sup>2,6</sup> Considerable experimental effort has been made to elucidate the physics of these important defects.<sup>7</sup> However, there remain unresolved issues, even at the basic level of whether the metal impurities substitute at the A or B site, and whether they displace off-center to form dipoles at the respective sites.

One example where controversies linger is the location of some divalent metal substituents in  $\text{KTaO}_3$  and KTN (a solid solution of  $\text{KTaO}_3$  and  $\text{KNbO}_3$ ).  $\text{KTaO}_3$  is an incipient ferroelectric. The pure material remains paraelectric and retains a cubic symmetry down to zero temperature.<sup>8</sup> So this material lends itself to studying impurity dipoles without the complication of intervening phase transitions. KTN exhibits a ferroelectric phase when the Nb concentration reaches  $\sim 2\%$ .<sup>9,10</sup> When paramagnetic  $\text{Mn}^{2+}$  is doped into  $\text{KTaO}_3$ , the electron-spin-resonance (ESR) technique can in principle be used to determine the impurity substitution site and dipole orientation. The crystal fields at the A (K) and B (Ta) sites are distinct, and  $\text{Mn}^{2+}$  residing at each site should give fine structures that characterize the defect environment. But so far,

experiments have yielded contradictory interpretations. Hannon,<sup>11</sup> Bykov *et al.*,<sup>12</sup> and Abraham *et al.*<sup>13</sup> conclude that  $\text{Mn}^{2+}$  substitutes at the B site (henceforth referred to as  $\text{Mn}_{\text{Ta}}$ ), inducing a captive oxygen vacancy ( $V_{\text{O}}^{2+}$ ) in its first-neighbor shell. Recent work by Laguta and co-workers<sup>14</sup> and Laulicht *et al.*,<sup>15</sup> on the other hand, concludes that  $\text{Mn}^{2+}$  resides on the A site (i.e.,  $\text{Mn}_{\text{K}}$ ). This Mn displaces  $\sim 0.9$  Å in the (100) lattice direction, without any charge-compensating defect such as a K vacancy in the immediate neighborhood.<sup>14</sup>  $\text{Mn}^{2+}$  goes into the B-site in the closely related incipient ferroelectric  $\text{SrTiO}_3$ . However, attempts to apply this conclusion to  $\text{KTaO}_3$  have been controversial.<sup>16,17</sup>

Tracking ESR spectra as a function of temperature provides further information about the impurity environment. At elevated temperature, the fine structure splitting vanishes,<sup>12,14</sup> signaling that the impurity dipole has acquired sufficient thermal energy to overcome the barrier for dipole reorientation to another symmetry-related direction. According to these experiments, an activation energy of 0.115 eV accompanies dipole reorientation in  $\text{KTaO}_3:\text{Mn}^{2+}$ . An impurity dipole reorientation barrier of 0.11 eV is also deduced from frequency-dependent dielectric relaxation measurements by Nowick *et al.*<sup>18</sup> The ESR work of Ref. 15 gives a barrier of 0.065 eV, which is measured in 3% Nb KTN solid solution. This value seems out of line with those measured in pure  $\text{KTaO}_3$ , and henceforth we will assume an experimental value of  $\sim 0.11$  eV for the reorientation activation energy in  $\text{KTaO}_3$ . Citing the early work of Bykov *et al.*,<sup>12</sup> Nowick *et al.* conclude that this barrier is associated with the hopping of an oxygen vacancy between two equivalent sites in the first-neighbor shell of Mn residing at the Ta site. This interpretation does not agree with the more recent work of Ref. 14.

The possibility of multiple charge states in transition ions such as Mn brings complications when one attempts to determine the most stable defect structure(s). In view of this, recent experiments on Ca-doped KTN (Ref. 19) and  $\text{KTaO}_3:\text{Ba}$  (Ref. 20) are especially illuminating. In the KTN:Ca sample in question (2.3% Nb, 0.055% Ca), the small amount of Ca added significantly increases the Curie

temperature.<sup>19</sup> This suggests that Ca substituents create dipoles that couple strongly to the ferroelectric host. The dielectric loss spectra is consistent with activated dynamics with an activation energy of 0.08 eV. The magnitude of this barrier is comparable to the one observed in  $\text{KTaO}_3:\text{Mn}^{2+}$ . This signature is absent for pure KTN samples.<sup>21</sup> Given these observations, a comparative theoretical study of Ca and Mn impurities should shed light on the structure and dynamics of dipolar defects in  $\text{KTaO}_3$ , and perhaps in perovskites in general.

In this paper, we apply first-principles methods to study the energetics, structures, and dynamics associated with  $\text{Ca}^{2+}$  and  $\text{Mn}^{2+}$  impurities in cubic  $\text{KTaO}_3$ . There have been relatively few first-principles calculations on defects in perovskites, especially in  $\text{KTaO}_3$ . Exner *et al.*<sup>22</sup> have compiled a list of formation energies and favorable solid-state chemical reactions for incorporating a series of mono-, di-, and trivalent substituents, using a shell model for the ions. Li and Na impurities have been examined using the full potential linear muffin-tin orbital (LMTO) method.<sup>23</sup> Li (Ref. 24) and Nb (Refs. 25 and 26) substituted at the K and Ta sites, respectively, have also been studied using a semiempirical Hartree-Fock method. However, the full potential method used in Ref. 23 gave results that exhibit discrepancies with all-electron linearized augmented plane wave (LAPW) local density approximation (LDA) first-principles predictions, particularly with regard to the soft phonon modes in pure  $\text{KTaO}_3$ .<sup>27</sup> More recently, first-principles studies of Pt impurities,<sup>6</sup> Pb vacancies,<sup>28</sup> and O vacancies<sup>29</sup> in  $\text{PbTiO}_3$  have been performed. This list, by no means exhaustive, highlights the value of performing more first-principles studies to benchmark semiempirical calculations.

The present work on Ca-substituent energetics follows the framework of Ref. 22, but applies density functional theory instead of empirical models. We also consider the activation energies for oxygen vacancy hopping within the first-neighbor shell of the Ta-site substituents, as well as the dynamics involving Mn and Ca motion at the K sites. While the system is ionic and its structural properties should be reasonably well treated within the shell model of Ref. 22, the predictions for dynamics can be sensitive to the parameters used in empirical models. With our test cases of  $\text{KTaO}_3:\text{Ca}$  and  $\text{KTaO}_3:\text{Mn}$ , we hope to provide a useful first-principles paradigm for dipole reorientation dynamics in ferroelectric perovskites.

The paper is organized as follows. Section II describes the details of the first-principles implementation. Validation of this implementation is given in Sec. III, where special attention is paid to the convergence of defect formation energies with supercell dimensions. Sections IV and V discuss the predictions for impurity incorporation energetics and dipole reorientation dynamics, respectively, and Sec. VI concludes the paper with further discussion.

## II. METHOD

The calculations are performed using the Vienna atomic simulation package<sup>30</sup> (VASP), which utilizes ultrasoft pseudopotentials.<sup>31</sup> The LDA approximation<sup>32</sup> for the ex-

change correlation functional is used. When unpaired electrons are present, the spin-polarized local density functional approximation<sup>33</sup> (SLDA) is applied instead. The generalized gradient approximation<sup>34</sup> (GGA) to the exchange correlation function, which has been known to give diffusion barriers closer to experimental values in some insulators,<sup>35</sup> is also applied to provide a consistency test for determining activation energies. The pseudopotentials for K, Ca, and Mn include pseudovalent  $p$ -shell electrons. The defect structures are computed using periodically replicated supercells of varying sizes. To compute defect formation energies, the Brillouin zones of these supercells are sampled using Monkhorst-Pack grids<sup>36</sup> equivalent to or denser than  $6 \times 6 \times 6$   $k$  points within one primitive cell.  $4 \times 4 \times 4$  sampling is used for most of the dipole reorientation activation energy results. All calculations are performed at the equilibrium LDA or GGA lattice constants, as the case might be, except where indicated. To compute the activation energy of dipole reorientation, the nudged elastic band (NEB) method<sup>37-40</sup> is applied. This method will be discussed in more detail in Sec. V.

The designations  $\text{Ca}^{2+}$ ,  $\text{Mn}^{2+}$ , and  $\text{V}_\text{O}^{2+}$  used in this work refer to nominal ionic charges. Operationally, when we replace a K atom with Ca, the total number of electrons in the simulation cell is adjusted such that K, Ca, Mn, Ta, and O ions have ionic charges of +1, +2, +2, +5, and -2, respectively. For example, the Ca pseudopotential accounts for six pseudovalent  $3p$  electrons in addition to two  $4s$  electrons. A nominal “ $\text{Ca}^{2+}$ ” ion thus contributes six net electrons to the simulation cell. Similarly, the oxygen pseudopotential is associated with two  $2s$  and four  $2p$  electrons, and thus a “ $\text{V}_\text{O}^{2+}$ ” oxygen vacancy eliminates eight electrons from the cell. With this procedure, the supercells with Ca defects are insulators and do not have impurity states in the band gap. (However, the transition-metal Mn defects do exhibit such impurity states.) When  $\text{Ca}^{2+}$  or  $\text{Mn}^{2+}$  substitutes for  $\text{K}^+$  or  $\text{Ta}^{5+}$ , the supercell cell that represents isolated defects will have a net charge (even in the presence of oxygen vacancy), which is not compatible with the periodic boundary conditions used in this work. In those cases, overall charge neutrality is preserved by adding a compensating, uniform background charge to the supercell. This will be discussed further in Sec. III B.

## III. ACCURACY AND CONVERGENCE TESTS

To determine the defect structures and dynamics, accurate formation energies and barrier heights are required. First-principles predictions are far more reliable than semiempirical results for this purpose. However, the high cost of these calculations limits the size of supercells that can be used to mimic isolated defects. The convergence behavior with respect to cell size is discussed in detail in this section.

### A. Validation of LDA and pseudopotentials

The ultrasoft pseudopotentials used herein, in conjunction with LDA, gives a lattice constant of 3.957 Å for  $\text{KTaO}_3$ , which is 0.6% smaller than the experimental lattice constant

TABLE I. Comparison of predicted phonon frequencies with LAPW results computed at experimental lattice constant (Ref. 27) and experimental results (Ref. 42) extrapolated to zero temperature (Ref. 27).

Mode	VASP (expt. $a_0$ )	VASP (LDA $a_0$ )	LAPW <sup>a</sup>	Experiment <sup>b</sup>
TO <sub>2</sub>	85.8 cm <sup>-1</sup>	117.8 cm <sup>-1</sup>	80 cm <sup>-1</sup>	24 cm <sup>-1</sup>
TO <sub>3</sub>	193.9 cm <sup>-1</sup>	204.8 cm <sup>-1</sup>	172 cm <sup>-1</sup>	197 cm <sup>-1</sup>
TO <sub>4</sub>	276.0 cm <sup>-1</sup>	273.3 cm <sup>-1</sup>	264 cm <sup>-1</sup>	274 cm <sup>-1</sup>
TO <sub>5</sub>	555.4 cm <sup>-1</sup>	582.1 cm <sup>-1</sup>	529 cm <sup>-1</sup>	546 cm <sup>-1</sup>

<sup>a</sup>Reference 27.

<sup>b</sup>Reference 42.

and is in excellent agreement with the 3.96 Å obtained using LAPW.<sup>27</sup> GGA predicts a lattice constant of 4.027 Å, which is in excellent agreement with the GGA results of Ref. 41 and is 1% larger than the experimental value. As a further validation of the pseudopotentials, Table I lists the  $\Gamma$ -point phonon frequencies computed at both LDA and experimental lattice constants. Also shown are the LAPW results computed at experimental lattice constant<sup>27</sup> and experimental phonon frequencies<sup>42</sup> extrapolated to zero temperature in Ref. 27. The close agreement between our phonon frequencies and LAPW results demonstrates that our ultrasoft pseudopotential implementation closely mimics all-electron LDA despite the omission of inner-shell electrons in the Ta pseudopotential.

The soft TO mode frequency differs from the experimental value by 60 cm<sup>-1</sup> at the experimental lattice constant, and by as much as 94 cm<sup>-1</sup> at the LDA lattice constant. This frequency, which is close to vanishing, is proportional to the square root of the lowest eigenvalue of the dynamical matrix and is sensitive to small errors in lattice constants. The disagreement with experimental force constant should not be considered excessive. However, it does indicate that the system at its LDA lattice constant is farther away from criticality than experimental  $\text{KTaO}_3$ . LDA  $\text{KTaO}_3$  will therefore exhibit a lower static dielectric constant  $\epsilon_0$  as well as a smaller correlation length. Assuming a linear dielectric effective medium for the host  $\text{KTaO}_3$ , this will cause a small uncertainty in the absolute solvation energy of charged species, which, depending on the ionic radius, can be a few tenths of an electron volt for highly charged defects. As a result, the binding energy between oppositely charged defects may be somewhat unreliable if the species are highly charged.

In general, LDA equilibrium structures are reliable for perovskites. On the other hand, LDA has been known to give diffusion barriers that are off by 33%, while GGA has been known to be off by 20%.<sup>35</sup>

### B. Convergence with respect to cell size

Too small a supercell causes artificial strain fields and periodic charge arrays that stem from the artificial periodic boundary conditions. In this work, the effect of image charges is controlled by adding a monopole Madelung

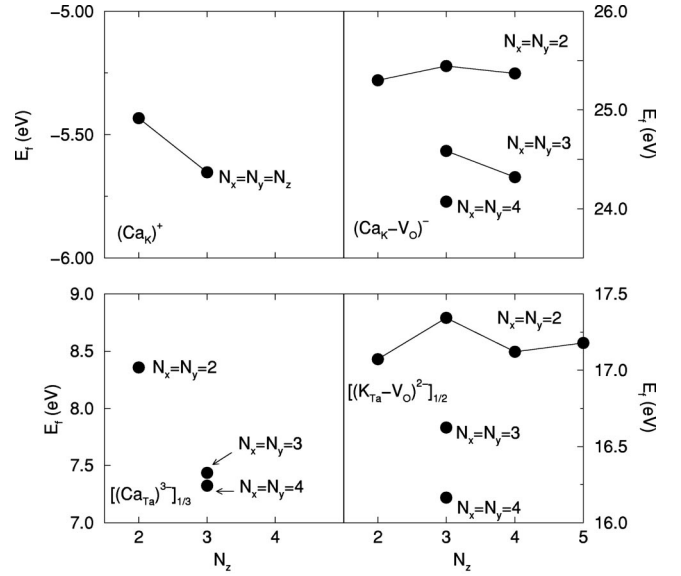


FIG. 1. Convergence of defect formation energy  $E_f$  for  $\text{Ca}_K^+$ ,  $(\text{Ca}_{\text{Ta}}-\text{V}_O)^-$ ,  $\text{Ca}_{\text{Ta}}^{3-}$ , and  $(\text{K}_{\text{Ta}}-\text{V}_O)^{2-}$ . The defect charges indicated in this and all subsequent figures derives from valence electron counting, not from examination of the electron density distributions.  $E_f$  is normalized with respect to the charge in the supercell. The lines and circles are guides to the eye. A convergence of  $\sim 0.25$  eV is attained for the Ca impurities, while K substituting at the Ta site, bound to an oxygen vacancy, converges poorly because of the large relaxation of the K atom. Fortunately, this complex proves too energetically costly to be a viable defect structure.

correction.<sup>43</sup> The LDA high-frequency dielectric constant is required for this correction. We assume  $\epsilon_\infty^{\text{LDA}} = 5.115$ , which is 10% larger than the experimental value of 4.65.<sup>44</sup> The monopole and dipole interactions among supercell images can in principle be completely eliminated using a reference charge distribution technique.<sup>45,46</sup>

Figure 1 depicts the convergence behavior as a function of supercell size. The defect formation energy  $E_f$  for several structures we will investigate in Sec. IV is plotted against the cell dimensions  $(N_x, N_y, N_z)$  along the three Cartesian directions. We define  $E_f$  as the change in cohesive energy between the supercell containing the defect and an identical supercell consisting of perfect crystal  $\text{KTaO}_3$ .  $E_f$  is normalized for the charge in the supercell; Sec. IV will show that, for the purpose of determining the most favorable mode of incorporating Ca, this normalized energy is the relevant quantity. In general, the defect structures that do not involve oxygen vacancies are apparently converged to 0.25 eV per charge for  $N_x=3$ . However, when one (or more) oxygen vacancy exists in the first-neighbor shell of a large metal ion [e.g., in  $(\text{K}_{\text{Ta}}-\text{V}_O)^{2-}$ ], the metal displacement can exceed 1 Å. This induces large strain and leads to slow  $E_f$  convergence. As we will show,  $(\text{K}_{\text{Ta}}-\text{V}_O)^{2-}$  is not a low-energy defect, and therefore this does not prevent us from assigning the lowest-energy structures for Ca impurities (Sec. IV). In cases where cubic symmetry-breaking oxygen vacancies exist,  $E_f$  converges more slowly with cell size in the direction *perpendicular* to the direction of the metal- $\text{V}_O^{2+}$  dipole aligned in the  $z$ -direction, and up to  $4 \times 4$  sampling in the

transverse directions is used. This is despite the fact that the supercell is a well-behaved insulator that exhibits no states in the gap. We also note that our largest supercell of 240 atoms is 3 times as large as those used in first-principles LDA studies reported in the literature.<sup>6,28,29</sup>

#### IV. DEFECT STRUCTURES AND ENERGETICS OF Ca SUBSTITUENTS

##### A. Candidates for defect structures

Given the highly ionic nature of the species present in  $\text{KTaO}_3:\text{Ca}$ , we have focused on nominal ionic charges when considering possible defect structures. When substituting a  $\text{Ca}^{2+}$  for either  $\text{K}^+$  or  $\text{Ta}^{5+}$ , or when creating one oxygen vacancy by removing  $\text{O}^{2-}$ , charged defects are formed and the supercell cannot be kept neutral. The intrinsic defect concentration of  $\text{KTaO}_3$  is of order a few hundred parts per million,<sup>47</sup> and are not sufficient to accept excess electrons from (or donate them to) the extrinsic Ca-containing defects that want to be positively (negatively) charged. Therefore we assume that, whenever a positively charged defect is created by a impurity, a compensating negatively charged defect must exist to preserve overall charge neutrality.

The choices of possible low-energy defect structures are guided by a previous shell-model study.<sup>22</sup> The isolated positively charged defects examined are  $\text{Ca}_\text{K}^+$ ,  $(\text{V}_\text{K}-\text{V}_\text{O})^+$ ,  $[\text{Ca}_\text{Ta}-(\text{V}_\text{O})_2]^+$ , and  $\text{V}_\text{O}^{2+}$ . The candidates for isolated negatively charged defects are  $(\text{Ca}_\text{Ta}-\text{V}_\text{O})^-$ ,  $\text{V}_\text{K}^-$ ,  $(\text{K}_\text{Ta}-\text{V}_\text{O})^{2-}$ , and  $\text{Ca}_\text{Ta}^{3-}$ . Here the notation for charges indicated for each defect complex follows Ref. 22 and are based on valence charge counting (e.g.,  $\text{Ta}^{5+}$  replaced by  $\text{Ca}^{2+}$  gives  $\text{Ca}_\text{Ta}^{3-}$  in the *supercell*) rather than a careful study of the electronic density distribution around each ion. The electron density contour maps will be deferred to later studies. These notations also give the total compensating background charge used in the defect supercell.

Figures 2 and 3 depict some of these structures. Relatively small lattice relaxations is found in  $\text{Ca}_\text{K}^+$ . This defect does not have Ca residing off-center and therefore forms no dipoles. On the other hand, in  $(\text{Ca}_\text{Ta}-\text{V}_\text{O})^+$ , Ca displaces  $\sim 0.1 \text{ \AA}$  towards the oxygen vacancy in its first-neighbor shell, forming a large dipole. In  $\text{Ca}_\text{Ta}^{3-}$ , the large size of  $\text{Ca}^{2+}$  relative to the  $\text{Ta}^{5+}$  normally residing there forces the oxygen ions surrounding the cramped Ta site to displace outwards by  $0.17 \text{ \AA}$ . (The nearest-neighbor K-O distance in bulk  $\text{KTaO}_3$  is  $2.8 \text{ \AA}$ , compared to  $2 \text{ \AA}$  for Ta-O.) The  $\text{K}^+$  ion is even larger than  $\text{Ca}^{2+}$ ; as alluded to before, it displaces more than  $1 \text{ \AA}$  towards the oxygen vacancy that is bound to it at the Ta site.

To compute the solvation energy of Ca associated with each defect, we need to add or subtract the chemical potentials of each species added to or removed from the supercell, respectively. In the synthesis,<sup>11,19</sup>  $\text{Ta}_2\text{O}_5$  and excess  $\text{K}_2\text{CO}_3$  are heated to  $1000 \text{ K}$  in air.  $\text{K}_2\text{CO}_3$  is replaced by  $\text{K}_2\text{O}$  in our calculations since  $\text{CO}_2$  is readily eliminated from the carbonate. The chemical potentials  $\mu_\text{K}$ ,  $\mu_\text{Ca}$ , and  $\mu_\text{Ta}$  are determined from the cohesive energies of  $\text{K}_2\text{O}$ ,  $\text{CaO}$ , and  $\text{KTaO}_3$ .<sup>48</sup>  $\text{Ta}_2\text{O}_5$  is irrelevant here because it is the reactant

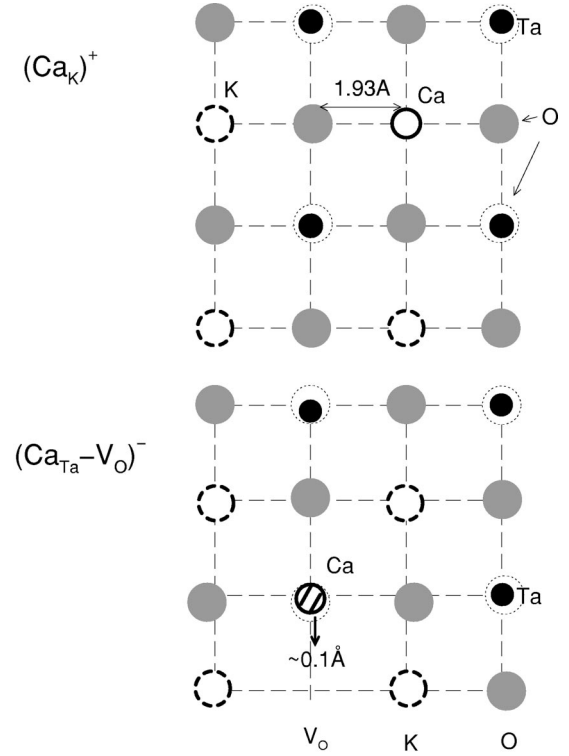


FIG. 2. Structures of  $\text{Ca}_\text{K}^+$  and  $(\text{Ca}_\text{Ta}-\text{V}_\text{O})^-$ , depicted as cross sections in the  $x$ - $y$  plane. The filled or shaded circles are in the Ta ( $B$ -site) layer while the open circles are coplanar with K ( $A$  site). The solid line circles represent Ca while circles with dashed lines are K atoms. These are shaded only if they are in the Ta layer. Ta are depicted as small, filled, black circles, while O atoms in the Ta and K layers are represented as filled gray circles and open circles with dotted lines, respectively. The  $\text{Ca}_\text{K}^+$  supercell has a cubic symmetry. Note that the Ta-O bond length for pure  $\text{KTaO}_3$  is  $1.98 \text{ \AA}$  according to LDA.  $(\text{Ca}_\text{Ta}-\text{V}_\text{O})^-$  exhibits  $C_{4v}$  symmetry, and  $\text{Ca}^{2+}$  is displaced by  $\sim 0.1 \text{ \AA}$  towards the oxygen vacancy.

assumed to be completely exhausted during synthesis. So, for example,  $E_\text{cohesive}^{\text{CaO}} = \mu_\text{Ca} + \mu_\text{O}$ .  $\mu_\text{O}$  can in principle be calculated from the partial pressure in air and the cohesive energy of  $\text{O}_2$  molecules.<sup>48</sup> Since mass is conserved and all ions retain their nominal charges,  $\mu_\text{O}$  can actually be eliminated in the final expression when defect pairs with equal but opposite charges are combined. Therefore  $\mu_\text{O}$  can be left unspecified. The solvation energies are referenced to constant  $\mu_\text{K}$ ,  $\mu_\text{Ca}$ ,  $\mu_\text{Ta}$ , and  $\mu_\text{O}$ . For instance,

$$E_\text{sol}^{\text{Ca}_\text{K}} = E_\text{f}^{\text{Ca}_\text{K}} - \mu_\text{Ca} + \mu_\text{K}.$$

Using these solvation energies, we search for the most stable pair of defects with equal and opposite charges. The possible structures are first screened using underconverged (i.e.,  $N_x = N_y = N_z = 2$ ) supercells; no attempt is made to further converge  $E_\text{f}$  for structures with very unfavorable energies. Table II confirms that some defects under consideration are evidently so costly they can be ignored. The most favorable structures are converged to  $\sim 0.25 \text{ eV}$  per charge. From Table II, we predict the most favorable solid-state reaction to be

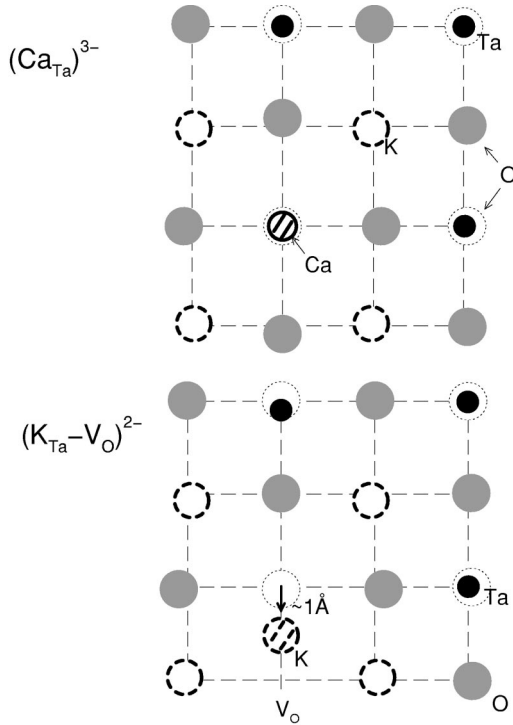
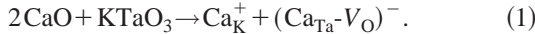
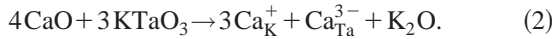


FIG. 3. Structures of  $\text{Ca}_{\text{Ta}}^{3-}$  and  $(\text{K}_{\text{Ta}}-\text{V}_{\text{O}})^{2-}$ . For a description of the symbols, see the caption of Fig. 2.



The nondipolar defect  $\text{Ca}_{\text{Ta}}^{3-}$  is only slightly higher in energy ( $\sim 0.3$  eV) per Ca impurity:



The stability of these two structures relative to other possible defects is in qualitative agreement with Ref. 22. Table II shows that potassium vacancies, which have been speculated to accompany  $\text{Ca}_{\text{K}}^+$  in the literature, are highly unfavorable. The trends in Table II can be rationalized in terms of ionic charges and sizes.  $\text{Ca}^{2+}$  substituting for  $\text{Ta}^{5+}$  creates a large localized charge in addition to forcing a larger ion into a congested Ta site. These Ta-site disadvantages can be alleviated by binding an oxygen vacancy to  $\text{Ca}_{\text{Ta}}^+$ . The  $\text{K}^+$  ion is simply too large to fit into the Ta site even with an oxygen vacancy in its first-neighbor shell. In the more stable  $(\text{Ca}_{\text{Ta}}-\text{V}_{\text{O}})^-$  defect, a dipole is formed. This appears to be

TABLE II. Solvation energy per Ca in various defect pairs. The defects marked by an asterisk and a dagger have  $E_f$  converged to 0.25 eV and 0.5 eV per charge, respectively. The other entries are computed using  $N_x=N_y=N_z=2$  supercells and  $2 \times 2 \times 2$  Monkhorst-Pack  $k$ -point sampling.

	$(\text{Ca}_{\text{K}})^{+*}$	$(\text{V}_{\text{K}}-\text{V}_{\text{O}})^+$	$[\text{Ca}_{\text{Ta}}-(\text{V}_{\text{O}})_2]^{+\dagger}$	$\text{V}_{\text{O}}^{2+}$
$(\text{Ca}_{\text{Ta}}-\text{V}_{\text{O}})^{-*}$	1.4 eV	7.7 eV	2.5 eV	4.4 eV
$(\text{Ca}_{\text{Ta}})^{3-*}$	1.7 eV	21.4 eV	3.4 eV	11.7 eV
$(\text{K}_{\text{Ta}}-\text{V}_{\text{O}})^{2-\dagger}$	2.4 eV	NA	4.7 eV	NA
$(\text{V}_{\text{K}})^{-*}$	3.4 eV	NA	5.7 eV	NA

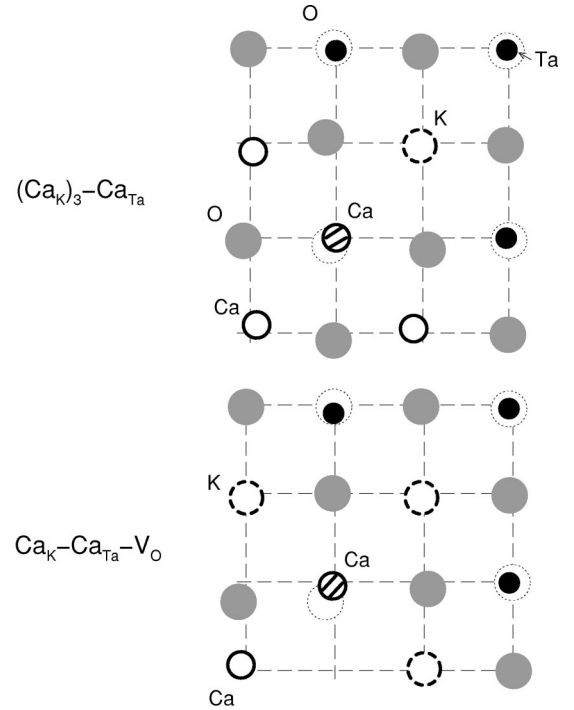


FIG. 4. Structures of two defect clusters,  $\text{Ca}_{\text{K}}-\text{Ca}_{\text{Ta}}-\text{V}_{\text{O}}$  and  $(\text{Ca}_{\text{K}})_3-\text{Ca}_{\text{Ta}}$  (see text). For a description of the symbols, see the caption of Fig. 2.

consistent with the experimental observation that Ca stabilizes the ferroelectric phase in KTN.<sup>19</sup>

Our theoretical treatment differs from experiments in that 2.3% Nb actually exists in the KTN:Ca sample in question.<sup>19</sup> This amount of Nb is sufficient to cause a paraelectric-to-ferroelectric phase transition.<sup>9,10</sup> Our first-principles implementation, which uses the LDA,<sup>32</sup> overestimates the frequency of the soft optical mode (see Sec. III A and Ref. 27). It is difficult to treat the phase transition and the accompanying lattice distortions induced by such a small amount of Nb, because a large supercell is needed to account for the proper composition, and because the small error in LDA lattice constant may preclude an extremely accurate prediction of the phase boundary. Furthermore, the breaking of cubic symmetry that accompanies phase transitions in KTN will give rise to a much larger number of possible defect structures separated by small energies, compared to the case in high-symmetry  $\text{KTaO}_3$ . To restrict ourselves to studying generic features of defects, we have chosen cubic  $\text{KTaO}_3$  as the host lattice.

## B. Defect clustering

Since the defects are charged, clustering is favored electrostatically and is a distinct possibility. We have investigated two possible charge-compensated complexes,  $(\text{Ca}_{\text{K}})_3-\text{Ca}_{\text{Ta}}$  and  $\text{Ca}_{\text{K}}-\text{Ca}_{\text{Ta}}-\text{V}_{\text{O}}$ , which are depicted in Fig. 4. Within the precision of the calculation, no binding energy is observed between the bound pair of  $\text{Ca}_{\text{K}}^+$  and  $(\text{Ca}_{\text{Ta}}-\text{V}_{\text{O}})^-$ . On the other hand, because  $\text{Ca}_{\text{Ta}}^{3-}$  carries a large charge, a binding energy of 3.0 eV obtains for  $(\text{Ca}_{\text{K}})_3-\text{Ca}_{\text{Ta}}$ . This

translates into a 0.75 eV decrease in energy per Ca substituent in Eq. (2), which will put this complex 0.35 eV lower in energy per Ca than the isolated  $\text{Ca}_K^+$  and  $(\text{Ca}_{\text{Ta}}-\text{V}_\text{O})^-$  pair [Eq. (1)].

The  $(\text{Ca}_K)_3\text{-Ca}_{\text{Ta}}$  cluster carries a dipole that cannot readily reorient at low temperature. It is unlikely to be responsible for the temperature-dependent dielectric loss signature. Experimentally, the synthesis is carried out at  $T = 1000$  K, and the configurational entropy cost of assembling four impurity atoms has to be considered when determining whether Ca clustering can occur. During crystal growth, CaO is spontaneously incorporated into  $\text{KTaO}_3$ ,<sup>47</sup> which suggests that the solid-state reaction that incorporates Ca has a negative free energy. Our calculations always give positive incorporation energy at zero temperature. Barring large LDA errors in cohesive energies, entropy must play a large role in determining the defect structure. As we have not systematically varied the cluster size, shape, and orientation, the possible effect of clustering on dipole formation and dynamics will be deferred to future studies.

## V. DIPOLE REORIENTATION DYNAMICS

The calculations of dipole orientation barriers are performed from first principles using multidimensional transition state theory.<sup>49</sup> Here the relevant barrier height is the lowest saddle point separating the initial and final configurations in the potential energy landscape comprising all atomic degrees of freedom in the supercell. In our case, the initial/final configurations are two of the possible orientations of (say) the  $(\text{Ca}_{\text{Ta}}-\text{V}_\text{O})^-$  dipole. An efficient algorithm for finding this saddle point is the NEB method.<sup>37</sup> This method creates a series of replicas along the reorientation (or “reaction,” to borrow physical chemistry terminology) path that interpolates between the initial (reactant) and final (product) configurations. An energy function is introduced to penalize large changes of atomic coordinates between nearest neighbors in replica space. The reaction path is found by minimizing a suitable action that governs all degrees of freedom in the replicas, subject to the constraint that the path passes through a saddle point;<sup>37</sup> the latter then is obtained via interpolation. This general, robust method has been implemented within the VASP package<sup>30</sup> and successfully applied to predict nontrivial reaction pathways.

Recent advances in NEB, namely the “climbing image” option,<sup>39,40</sup> deposits one image or replica along the reaction path such that atoms in that replica experience zero forces. In other words, this variation locates the saddle point without the need for interpolation. It facilitates computing barrier heights in systems with steep potential energy surfaces, and will also be used to investigate the energy barriers associated with oxygen vacancy hopping.

These algorithms will be used as the standard in activation energy calculations, against which simpler approaches will be compared.

### A. Oxygen vacancy hopping around $\text{Ca}_{\text{Ta}}^+$ and $\text{Mn}_{\text{Ta}}^+$

Our previous results suggest that  $\text{Ca}^{2+}$  resides in both K and Ta sites. First we consider the activation energy for di-

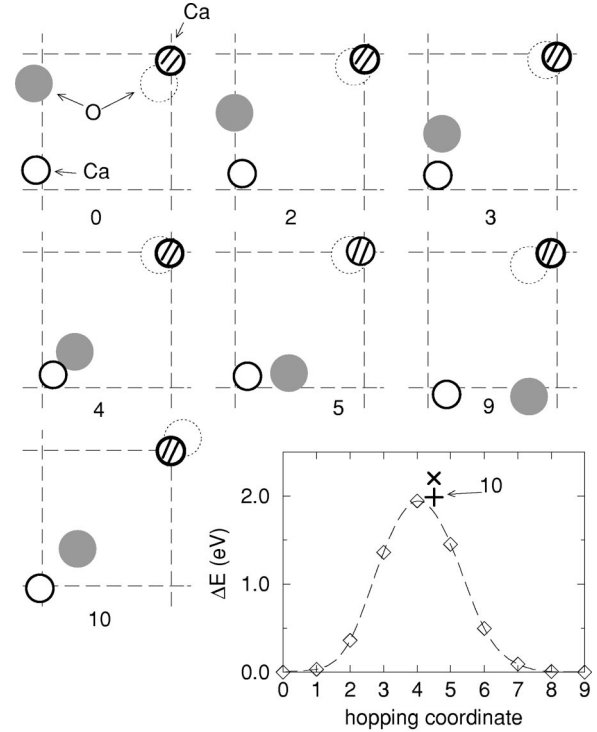


FIG. 5. Oxygen vacancy hopping pathway between symmetry-related, equivalent minima in  $(\text{Ca}_{\text{Ta}}-\text{V}_\text{O})^-$  computed using the NEB method with “climb” option and eight replicas (see text). The symbols are described in Fig. 2. In the inset, the activation energy profile is plotted as a function of the reaction coordinate (i.e., replica number within NEB). Diamonds are the total energies of the respective replicas referenced to the formation energy of the stable defect (panels 0 and 9). The dashed line is a spline fit. The plus and cross indicate the barrier height computed by imposing symmetry about the  $x=y$  plane (panel 10) for supercells of size  $N_x=N_y=N_z=2$  and  $N_x=N_y=N_z=3$ , respectively.

pole reorientation via oxygen vacancy hopping within the first-neighbor shell of Ca at the Ta site. Figure 5 depicts the lowest-energy  $\text{V}_\text{O}^{2+}$  hopping pathway in a  $(\text{Ca}_K\text{-Ca}_{\text{Ta}}-\text{V}_\text{O})^-$  complex, obtained using the climbing image NEB.<sup>39,40</sup> This doubly substituted supercell has been chosen as a paradigm because this cell is uncharged and does not suffer from artificial interactions between periodic image charges. A  $N_x=N_y=N_z=2$  supercell with  $2 \times 2 \times 2$   $K$ -grid sampling is used. With the “climb” option, the replica in panel 4 of Fig. 5 has the highest energy and it is thus a saddle point of the potential energy surface. We have confirmed that atomic forces are indeed zero in this configuration. The barrier to reorientation is predicted to be 1.945 eV (Table III). The oxygen atom, which undergoes hopping, stays within 0.2 Å of the Ta-containing lattice plane. The Ca atom at the K site also undergoes displacive motion; in panel 4, it displaces  $\sim 0.2$  Å off the  $x$ - $y$  plane, which contains the A site.

At present NEB is used with an even number of replicas. The climbing image option, which puts one replica at the saddle point, necessarily gives a nonsymmetry pathway as a function of the replica number. If this option is turned off, we find that the hopping pathway is apparently symmetric about the  $x=y$  plane (not shown).<sup>50</sup> This suggests that the

TABLE III. Dipole reorientation activation energy ( $\Delta E^\ddagger$ ) computed by imposing reflection symmetry about the  $x=y$  plane as well as by using the climbing image nudged elastic band method. The overall charge of the defect structures are omitted (see text).  $2 \times 2 \times 2$  Monkhorst-Pack  $k$ -point grids are used throughout. All activation energies are computed using LDA except where noted.

Defect	$N_x \times N_y \times N_z$	$\Delta E^\ddagger$ (eV): symmetry	$\Delta E^\ddagger$ (eV): climb NEB
$\text{Ca}_K\text{-Ca}_{\text{Ta}}\text{-V}_O$	$2 \times 2 \times 2$	1.988	1.945
$\text{Ca}_K\text{-Ca}_{\text{Ta}}\text{-V}_O$	$3 \times 3 \times 3$	2.204	NA
$\text{Ca}_{\text{Ta}}\text{-V}_O$	$2 \times 2 \times 2$	2.749	2.755
$\text{Ca}_{\text{Ta}}\text{-V}_O$	$3 \times 3 \times 3$	3.198	NA
$\text{Ca}_{\text{Ta}}\text{-V}_O$ (GGA)	$2 \times 2 \times 2$	2.611	NA
$\text{V}_O$	$2 \times 2 \times 2$	1.006	1.082
$\text{K}_{\text{Ta}}\text{-V}_O$	$2 \times 2 \times 2$	3.965	3.994
$\text{Mn}_{\text{Ta}}\text{-V}_O$	$2 \times 2 \times 2$	2.220	2.115
$\text{Mn}_K$	$2 \times 2 \times 2$	0.125	NA
$\text{Mn}_K$	$3 \times 3 \times 3$	0.182	NA

$x=y$  plane may be a dividing surface between reactant and product. To investigate this, we impose reflection symmetry about the  $x=y$  plane in this supercell in panel 10 and allow all other degrees of freedom to relax. Upon slightly breaking the symmetry about the  $x=y$  plane, the configuration in panel 10 relaxes to the stable defect structures. This confirms that panel 10 is indeed a saddle point, not a metastable structure. The energy difference between this constrained configuration and the stable defect structure is 1.988 eV (Table III). This energy difference is within 0.043 eV of the activation energy obtained with climbing image NEB. Thus, energetically speaking, the symmetric structure in panel 10 seems to be the saddle point for dipole reorientation. However, it is evident from Fig. 5 that the atomic positions in panels 4 and 10 can differ. The positions of the oxygen atom undergoing the hopping motion differ by  $\sim 0.04$  Å in the two panels, while the oxygen coordinates near the adjacent Ta site differ by as much as 0.34 Å. The LDA potential energy landscape near the saddle point is apparently sufficiently flat but complex that both of these slightly different structures are viable saddle point candidates, giving zero forces and essentially identical activation energies for dipole reorientation. If climbing image NEB with *odd* number of replicas were used, we believe panel 10 would result as the saddle point. Note that a saddle point with reflection symmetry is also predicted in  $\text{KNbO}_3$ , a closely related system.<sup>52</sup>

The qualitative features discussed above hold in all cases of oxygen vacancy hopping we have studied. Table III confirms that climbing image NEB gives dipole reorientation activation energies that are within 7% of  $x=y$  plane symmetry-constrained relaxation<sup>51</sup> for various defect complexes. Increasing the cell size to  $N_x=N_y=N_z=3$  increases the barrier by 0.2–0.45 eV. We have also compared one LDA result against the GGA prediction computed at the GGA lattice constant of  $\text{KTaO}_3$ . The difference is 0.14 eV, which is already smaller than the error due to using small supercells. We further note that the defect with the largest

metal ion displacement at the Ta site, namely  $(\text{K}_{\text{Ta}}\text{-V}_O)^{2-}$  (see Fig. 3), also exhibits the largest hopping barrier.

From Table III, we conclude that both climbing image NEB and relaxing the atom positions while preserving reflection symmetry about the  $x=y$  plane give very similar dipole reorientation activation energies. The atomic configuration at the saddle point can differ by up to  $\sim 0.3$  Å, and climbing image NEB does not unambiguously assign the saddle-point symmetry. Either method is sufficient to predict the energetics. However, the reflection symmetry method is particularly valuable because it is much less computationally demanding and allows convergence tests with respect to supercell size.

It is noteworthy that we predict an  $\sim 1$  eV barrier for intrinsic  $\text{V}_O^{2+}$  hopping in undoped  $\text{KTaO}_3$ , in agreement with experiments.<sup>53</sup> On the other hand, this value is in substantial disagreement with the 0.07 eV activation energy in pure  $\text{KTaO}_3$  predicted by the shell model of Exner *et al.*<sup>22</sup> Using NEB with up to eight replicas, we do not find the transition state *parallel* to the  $x=y$  plane that Ref. 22 apparently reports. This suggests that their shell model may not be as useful for dynamics as it apparently is for structural properties.<sup>52</sup>

All activation energies for  $\text{V}_O^{2+}$  hopping within the first-neighbor shell of  $\text{Ca}_{\text{Ta}}$  are predicted to exceed 2 eV. This is corroborated by the results of preliminary, constant temperature *ab initio* molecular dynamics simulations. Even at  $T=3000$  K, which corresponds to a thermal energy of  $\sim 0.25$  eV, the oxygen vacancy stays in the same lattice site after 2 ps of simulation. Therefore the oxygen vacancy hopping barrier must be significantly larger than 0.1 eV. We conclude that  $\sim 0.1$  eV activation energy deduced from dielectric loss measurements in  $\text{KTN}:\text{Ca}$  is most likely not associated with oxygen vacancy hopping. Note that this finding does not imply that  $(\text{Ca}_{\text{Ta}}\text{-V}_O)^-$  cannot exist; we have merely shown that  $(\text{Ca}_{\text{Ta}}\text{-V}_O)^-$  should not contribute to the dynamics at low temperature.

To gain further insight into the dynamics, we turn our attention to  $\text{Mn}^{2+}$  impurities, which are more amenable to experimental studies because of unpaired electrons. Since Mn readily takes on numerous charge states, searching for the most favorable defect pairs will be even more difficult than for Ca. Instead of attempting to predict the favorable structure(s), we explicitly consider the dynamics of isolated  $\text{Mn}_K^+$  and  $(\text{Mn}_{\text{Ta}}\text{-V}_O)^-$  and determine which defect is consistent with the activation energy observed in ESR and dielectric loss spectroscopies. As the supercell contains an odd number of electrons, SLDA is used in the computation. The  $\text{V}_O^{2+}$  hopping barrier within the first-neighbor shell of  $\text{Mn}_{\text{Ta}}^+$  is computed by imposing the aforementioned symmetry constraint and by climbing image NEB. As in all previous cases that involve oxygen vacancy hopping, the activation energy exceeds 1 eV (Table III). This finding seems to explicitly contradict the oft-cited assertion of Ref. 12, namely, that oxygen vacancy hopping around  $\text{Mn}_{\text{Ta}}^+$  exhibits a 0.11 eV barrier.

### B. Mn hopping motion at the K site

In this section, we investigate the possibility that  $\text{Mn}_K^+$  is responsible for the 0.11 eV activation energy, as suggested in

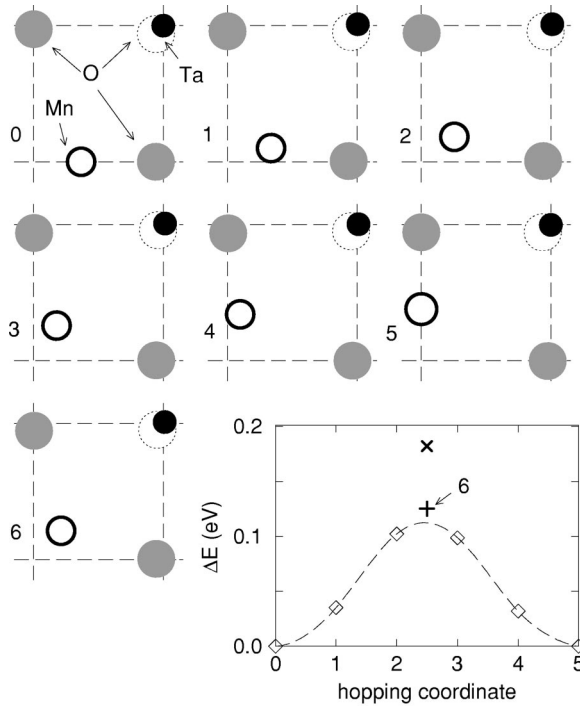


FIG. 6. Lowest-energy  $\text{Mn}^{2+}$  hopping pathway between symmetry-related  $\text{Mn}_K^+$  minima computed using LDA. The symbols are as in Fig. 5 except that Mn now replaces Ca and four replicas are used. The purpose of showing the underconverged barrier height (plus) is to demonstrate that the symmetry constraint prediction agrees well with the NEB method applied at identical cutoffs.

Refs. 12 and 14. Figure 6 shows that  $\text{Mn}^{2+}$  spontaneously displaces off center by  $0.81 \text{ \AA}$  along the (100) direction, which compares favorably with the  $0.9 \text{ \AA}$  displacement deduced from an anharmonic model analysis of ESR results.<sup>14</sup> The off-center motion of  $\text{Mn}^{2+}$  is in contrast to  $\text{Ca}^{2+}$ , which exhibits no such displacement. One difference between the two cases is the change in ionic radius, between  $0.99 \text{ \AA}$  for  $\text{Ca}^{2+}$  and  $0.80 \text{ \AA}$  for  $\text{Mn}^{2+}$ . Smaller ions are more likely to sit off-center at the A site; however, the stronger covalent bonding between the transition-metal ion  $\text{Mn}^{2+}$  and oxygen atoms should also play a role. The use of SLDA is crucial here. With LDA, the atoms relax to a configuration where Mn is displaced along (100) by  $1.4 \text{ \AA}$ . This alternative structure turns out to be metastable when SLDA is applied. On the other hand, the structure predicted by SLDA is unstable when LDA is used.

Next, the hopping of off-center  $\text{Mn}^{2+}$  between two of the six equivalent directions is investigated (Table III). The hopping path is apparently symmetric with respect to reflection about the  $x=y$  plane and the barrier appears to lie on the  $x=y$  dividing surface. The hopping species (Mn in this case) moves in the  $x$ - $y$  plane that contains the A site. However, the barrier is now predicted to be  $0.182 \text{ eV}$  when a  $N_x=N_y=N_z=3$  supercell is used.<sup>54</sup> This dipole reorientation activation energy is within a factor of two of known experimental values, compared to the factor of twenty discrepancy in the case of  $\text{V}_O^{2+}$  hopping. The large difference in  $\text{Mn}_K^+$  and  $\text{V}_O^{2+}$  hopping barriers in  $\text{KTaO}_3:\text{Mn}$  can be attributed to the fact

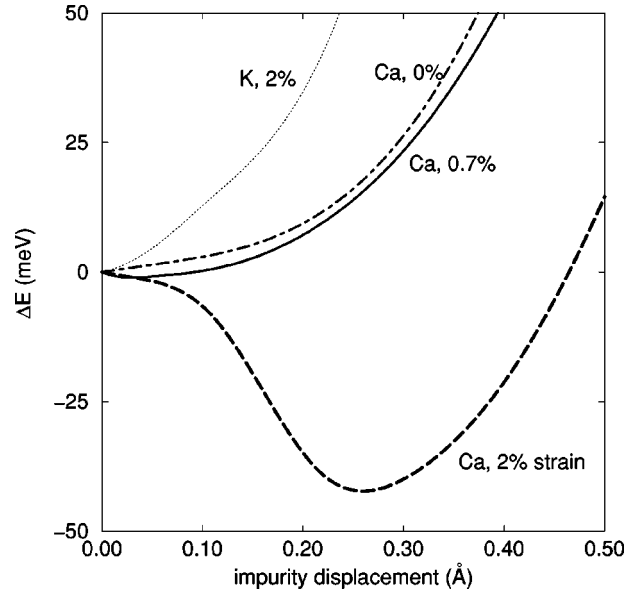


FIG. 7. Effect of uniaxial strain on Ca and K off-center displacement in the (100) direction at the A site. Dot-dashed line: Ca, 0% strain; solid line: Ca, 0.7%; dashed line: Ca, 2%; dotted line: K, 2%. These lines are spline fits to LDA results. The supercell volume is kept constant as the strain varies.

that the K site is much less congested than the Ta site, as mentioned above. Hence  $\text{Mn}^{2+}$  motion around the K site should be much less hindered than oxygen motion around the Ta site. Indeed, comparing the hopping pathways in Figs. 5 and 6 shows that oxygen vacancy hopping is accompanied by significant motion of several other atoms, whereas the Mn motion barely perturbs its nearest neighbors. Our prediction of a small barrier at the K site is reminiscent of the  $55 \text{ meV}$  gained in  $\text{Li}_K$  off-center displacement computed for an isolated Li impurity using full potential LMTO calculations, which necessarily implies that the LMTO hopping barrier for  $\text{Li}_K$  cannot exceed  $55 \text{ meV}$ .<sup>23,55</sup> Even though the convergence of the activation energy with supercell size is slow (Fig. 6), we can conclude that the experimentally observed  $\sim 0.1 \text{ eV}$  activation energy in experiments is consistent with the hopping motion of  $\text{Mn}_K^+$ .

### C. Conjecture on hopping dynamics in KTN:Ca

Unlike  $\text{Mn}_K^+$ ,  $\text{Ca}_K^+$  does not displace off-center and cannot directly be associated with the temperature dependence observed in dielectric loss spectroscopy. Our conjecture is that an off-center  $\text{Ca}^{2+}$  dipole obtains when Nb is also present at some of the Ta sites. Even though  $\text{Ca}^{2+}$  exhibits an unstable potential energy well centered at the K site, the potential surface is extremely flat. Figure 7 shows that an off-center displacement of  $0.2 \text{ \AA}$  in the (100) direction costs only  $7 \text{ meV}$ , provided all other atoms are relaxed to accommodate this motion. Recall that the 2.3% Nb concentration used in Ref. 19 is sufficient to cause a transition to the ferroelectric phase and a breaking of the cubic lattice symmetry. Even well above the Curie temperature, Nb substituents in  $\text{KTaO}_3$  displace off center<sup>56</sup> and cause lattice distortion

around them. They create strain fields that may perturb the flat energy surface for  $\text{Ca}_K^+$  sufficiently to create bistable potential wells, causing off-center motion. Since it is difficult to treat 2.3% Nb doping in a supercell (see the discussion in Sec. IV A), we elect to apply a tensile strain along the (100) direction at fixed supercell volume to test this hypothesis. The calculations are performed using  $N_x=N_y=N_z=2$  supercells with  $2 \times 2 \times 2$   $k$ -point sampling.

$\text{KNbO}_3$  has an orthorhombic crystal structure that exhibits a maximum tetragonal distortion of 1.7%,<sup>57</sup> while the maximum distortion for KTN at small Nb concentration is estimated to be less than 0.7%.<sup>58</sup> We find that, upon applying a 2% strain, Ca does become unstable at the K site. It displaces off-center in the (100) direction by  $\sim 0.26$  Å, forming a dipole and gaining  $\sim 43$  meV in the process (Fig. 7). This implies that a barrier of 43 meV now exists between dipoles in the (100) and  $(\bar{1}00)$  directions. A 0.7% uniaxial strain already causes off-center Ca displacement, albeit an extremely small one. Due to the small LDA error in soft-mode frequency and lattice constant, the LDA prediction of strain-induced Ca off-center displacement may not be extremely accurate.<sup>59</sup> Furthermore, convergence with cell size has not been pursued systematically. Within these uncertainties, we have nevertheless given a plausibility argument that off-center Ca displacement can be due to a sufficiently large uniaxial strain.

$\text{KTaO}_3:\text{Ba}$  does not exhibit the activated dielectric loss signature observed in  $\text{KTN}:\text{Ca}$ .<sup>20</sup> This is consistent with our argument that Nb is needed to create impurity dipoles, although it must be pointed out that the  $\text{Ba}^{2+}$  ion is much larger than  $\text{Ca}^{2+}$  and that difference will also affect the defect structure and dynamics. Pure KTN also lacks the activated signature seen in  $\text{KTN}:\text{Ca}$ . Comparing Ca at the A site with K in pure  $\text{KTaO}_3$ , we find that  $\text{K}^+$  sees a much steeper potential well. This difference is most likely due to the much larger ionic radius of  $\text{K}^+$ , which hinders off-center displacement. Using the 2% artificially strained cell mentioned above, we do not find any off-center  $\text{K}^+$  displacement (Fig. 7).

The presence of Nb will also change the  $V_O^{2+}$  hopping barrier around a  $\text{Ca}_{\text{Ta}}^{3-}$  impurity. However, it is extremely unlikely that Nb will lower the barrier to the  $\sim 0.1$  eV observed in experiments. Our various conjectures will be put to test in future experimental and theoretical works. Finally, while the conjecture about strain-induced off-center Ca dipoles appears reasonable, it should be pointed out that, in cases of more than one substituent such as that in  $\text{KTN}:\text{Ca}$ , interactions among substituent ions may lead to unexpected results. Unfortunately, systematic first-principles treatment of these complex systems is prohibitive at this time.

## VI. CONCLUSIONS

Pure  $\text{KTaO}_3$  is an ideal material for investigating defect structures and dynamics in perovskites because it retains its cubic symmetry down to zero temperature. We have considered  $\text{Ca}^{2+}$  and  $\text{Mn}^{2+}$  substituents in  $\text{KTaO}_3$  from first principles. We find that defect formation energies converge slowly with supercell size, especially in cases where oxygen vacancies are present and large relaxations of large ions at the Ta site (the B site in perovskites) entail. For Ca impurities,  $E_f$  generally converges to  $\sim 0.25$  eV using 135- and 240-atom cells in the absence and presence of oxygen vacancy, respectively. For the  $(\text{K}_{\text{Ta}}-\text{V}_O)^{2-}$  complex, on the other hand,  $E_f$  per defect has barely converged to the 1 eV level in a 240-atom supercell.

$\text{Ca}^{2+}$  substituting for  $\text{K}^+$  or  $\text{Ta}^{5+}$  necessarily creates charged defects, which must be compensated with oppositely charged extrinsic defects to preserve overall charge neutrality. Because of this, Ca goes into both K and Ta sites. For oppositely charged species far removed from each other, Ca at the Ta site is accompanied by an oxygen vacancy in its nearest-neighbor shell. The large electrostatic energy between highly charged defects favors clustering, which is not systemically investigated herein; it should be addressed in future studies that deal with impurities in perovskites.<sup>60</sup>

It is shown that the  $\sim 0.1$  eV activation energy deduced from ESR and dielectric loss measurements in  $\text{KTaO}_3:\text{Mn}^{2+}$  is consistent with dipole reorientation motion of off-center  $\text{Mn}_K$ , in agreement with recent experiments.<sup>14</sup> That is, the LDA-predicted hopping barrier is within 0.07 eV of the measured value. The experimental barrier is not consistent with  $V_O^{2+}$  hopping within the first-neighbor shell of  $\text{Mn}^{2+}$  substituting at the Ta site.  $\text{KTN}:\text{Ca}$  also exhibits a 0.08 eV activation energy in its dielectric loss spectra.<sup>19</sup> We argue that this dynamical signature is due to reorientation of off-center  $\text{Ca}^{2+}$  dipole at the K site; the off-center  $\text{Ca}^{2+}$  motion is speculated to arise from Nb-induced breaking of the cubic symmetry. In general, it appears that impurity ion hopping at the less congested A site exhibits a much smaller activation energy than oxygen vacancy hopping around the B site in  $\text{KTaO}_3$ . This conjecture will be tested for other impurities and for other perovskite hosts in future works.

## ACKNOWLEDGMENTS

We thank George Samara, Dwight Jennison, Alan Wright, Peter Feibelman, Tim Dunbar, Nicola Hill, and Georg Kresse for useful discussions, and Hans Jónsson and Grame Henkelman for graciously allowing us to use the climbing image nudged elastic band algorithm prior to its publication. This work was supported by the Department of Energy under Contract No. DE-AC04-94AL85000. Sandia is a multiprogram laboratory operated by Sandia Corporation, a Lockheed Martin Company, for the U.S. Department of Energy.

- <sup>1</sup>*Proceedings of the International Seminar on Relaxor Ferroelectrics* [Ferroelectrics **199**, 1 (1997)]; *Proceedings of the 1998 Williamsburg Workshop on Ferroelectrics* [*ibid.* **206&207**, 1 (1998)].
- <sup>2</sup>G.E. Pike, W.L. Warren, D. Dimos, B.A. Tuttle, R. Ramesh, J. Lee, V.G. Keramidis, and J.T. Evans, *Appl. Phys. Lett.* **66**, 484 (1995).
- <sup>3</sup>Qi Tan, Z. Xu, J.-F. Li, and D. Viehland, *Appl. Phys. Lett.* **71**, 1062 (1997).
- <sup>4</sup>T. Nakamura, Y. Nakao, A. Kamisawa, and H. Takasu, *Appl. Phys. Lett.* **65**, 1522 (1994).
- <sup>5</sup>G.A. Samara, *Ferroelectrics* **117**, 347 (1991), and references therein; L.E. Cross, *ibid.* **76**, 241 (1987).
- <sup>6</sup>S. Pöykkö and D.J. Chadi, *Phys. Rev. Lett.* **83**, 1231 (1999); *J. Phys. Chem. Solids* **61**, 291 (2000).
- <sup>7</sup>See U.T. Höchli, K. Knorr, and A. Loidl, *Adv. Phys.* **39**, 405 (1990) for a review of some impurity dipoles.
- <sup>8</sup>G.A. Samara and P.S. Peercy, in *Solid State Physics*, edited by H. Ehrenreich, F. Seitz, and D. Turnbull (Academic Press, New York, 1981), Vol. 36, p. 1 and references therein.
- <sup>9</sup>S. Triebwasser, *Phys. Rev.* **114**, 63 (1959).
- <sup>10</sup>D. Rytz, U.T. Höchli, and H. Bilz, *Phys. Rev. B* **22**, 359 (1980).
- <sup>11</sup>D.M. Hannon, *Phys. Rev. B* **3**, 2153 (1971).
- <sup>12</sup>I.P. Bykov, I.N. Geifman, M.D. Glinchuk, and B.K. Krulikovskii, *Fiz. Tverd. Tela (Leningrad)* **22**, 2144 (1980) [*Sov. Phys. Solid State* **22**, 1248 (1980)].
- <sup>13</sup>M.M. Abraham, L.A. Boatner, D.N. Olson, and U.T. Höchli, *J. Chem. Phys.* **81**, 2528 (1984).
- <sup>14</sup>V.V. Laguta, M.D. Glinchuk, I.P. Bykov, J. Rosa, L. Jastrabik, M. Sarinov, and Z. Trybula, *Phys. Rev. B* **61**, 3897 (2000).
- <sup>15</sup>I. Laulicht, Y. Yacobi, and A. Baram, *J. Chem. Phys.* **91**, 79 (1989).
- <sup>16</sup>R.A. Serway, W. Berlinger, K.A. Müller, and R.W. Collins, *Phys. Rev. B* **16**, 4761 (1977).
- <sup>17</sup>E. Siegel and K.A. Müller, *Phys. Rev. B* **19**, 109 (1979).
- <sup>18</sup>A.S. Nowick, S.Q. Fu, W.-K. Lee, B.S. Lim, and T. Scherban, *Mater. Sci. Eng.*, **B 23**, 19 (1994).
- <sup>19</sup>G.A. Samara and L.A. Boatner, *Phys. Rev. B* **61**, 3889 (2000).
- <sup>20</sup>G.A. Samara and L.A. Boatner (unpublished).
- <sup>21</sup>G.A. Samara, *J. Phys. Chem.* **94**, 1127 (1990).
- <sup>22</sup>M. Exner, H. Donnerberg, C.R.A. Catlow, and O.F. Schirmer, *Phys. Rev. B* **52**, 3930 (1995).
- <sup>23</sup>A.V. Postnikov, T. Neumann, and G. Borstel, *Ferroelectrics* **164**, 101 (1995).
- <sup>24</sup>R.I. Eglitis, A.V. Postnikov, and G. Borstel, *Phys. Rev. B* **55**, 12 976 (1997); *Phys. Status Solidi B* **209**, 187 (1998).
- <sup>25</sup>R.I. Eglitis, E.A. Kotomin, G. Borstel, and S. Dorfman, *J. Phys.: Condens. Matter* **10**, 6271 (1998).
- <sup>26</sup>V.S. Vikhnin, R.I. Eglitis, P.A. Markovin, and G. Borstel, *Phys. Status Solidi B* **212**, 53 (1999).
- <sup>27</sup>D.J. Singh, *Phys. Rev. B* **53**, 176 (1996).
- <sup>28</sup>S. Pöykkö and D.J. Chadi, *Appl. Phys. Lett.* **76**, 499 (2000).
- <sup>29</sup>C.H. Park and D.J. Chadi, *Phys. Rev. B* **57**, 13 961 (1998).
- <sup>30</sup>G. Kresse and J. Hafner, *Phys. Rev. B* **47**, 558 (1993); **49**, 14 251 (1994); G. Kresse and J. Furthmüller, *ibid.* **54**, 11 169 (1996).
- <sup>31</sup>D. Vanderbilt, *Phys. Rev. B* **41**, 7892 (1990).
- <sup>32</sup>W. Kohn and L.J. Sham, *Phys. Rev.* **140**, A1133 (1965).
- <sup>33</sup>U. von Barth and L. Hedin, *J. Phys. C* **5**, 1629 (1972); M.M. Pant and A.K. Rajagopal, *Solid State Commun.* **10**, 1157 (1972).
- <sup>34</sup>J.P. Perdew and Y. Wang, *Phys. Rev. B* **45**, 13 244 (1992); J.P. Perdew, J.A. Chevary, S.H. Vosko, K.A. Jackson, M.R. Pederison, D.J. Singh, and C. Fiolhais, *ibid.* **46**, 6671 (1992).
- <sup>35</sup>W.-K. Leung, R.J. Needs, G. Rajagopal, S. Itoh, and S. Ihara, *Phys. Rev. Lett.* **83**, 2351 (1999).
- <sup>36</sup>H.J. Monkhorst and J.D. Pack, *Phys. Rev. B* **13**, 5188 (1976).
- <sup>37</sup>G. Mills, H. Jönsson, and G.K. Schenter, *Surf. Sci.* **324**, 305 (1995).
- <sup>38</sup>G. Henkelman, G. Jóhannesson, and H. Jónsson, in *Progress on Theoretical Chemistry and Physics*, edited by S.D. Schwartz (Kluwer Academic, New York, 2000).
- <sup>39</sup>G. Henkelman, B.P. Uberauga, and H. Jónsson, *J. Chem. Phys.* **113**, 9901 (2000).
- <sup>40</sup>G. Henkelman and H. Jónsson, *J. Chem. Phys.* **113**, 9978 (2000).
- <sup>41</sup>S. Tinte, M.G. Stachiotti, C.O. Rodriguez, D.L. Novikov, and N.E. Christensen, *Phys. Rev. B* **58**, 11 959 (1998).
- <sup>42</sup>C.H. Perry, R. Currat, H. Buhay, R.M. Migoni, W.G. Stirling, and J. D. Axe, *Phys. Rev. B* **39**, 8666 (1989).
- <sup>43</sup>G. Makov and M.C. Payne, *Phys. Rev. B* **51**, 4014 (1995); G. Makov, R. Shah, and M.C. Payne, *ibid.* **53**, 15 513 (1996).
- <sup>44</sup>M. Didomenico and S.H. Wemple, *Phys. Rev.* **166**, 565 (1968); Y. Fujii and T. Sakudo, *J. Phys. Soc. Jpn.* **41**, 888 (1976). A 10% overestimation of  $\epsilon_\infty$  is typical of LDA calculations.
- <sup>45</sup>P.A. Schultz, *Phys. Rev. B* **60**, 1551 (1999); *Phys. Rev. Lett.* **84**, 1942 (2000).
- <sup>46</sup>A finite-sized cluster calculation does not contain the error due to periodic images, but the cluster size must exceed the equivalent of  $k$ -point sampling to properly represent the bulk crystal. In our case, a  $6 \times 6 \times 6$   $k$ -point sampling would mean a prohibitive cluster size of 216 primitive cells of 5 atoms each.
- <sup>47</sup>L.A. Boatner and G.A. Samara (private communications).
- <sup>48</sup>C. Stampfl and C.G. Van de Walle, *Appl. Phys. Lett.* **72**, 459 (1998).
- <sup>49</sup>For a review, see P. Hänggi, P. Talkner, and M. Borkovec, *Rev. Mod. Phys.* **62**, 251 (1990).
- <sup>50</sup>The climbing image option makes the NEB calculation much more robust for those defect supercells with reorientation activation energies exceeding 2 eV in the present cases.
- <sup>51</sup>Note that this symmetry constraint is viable in cubic  $\text{KTaO}_3$  but will be inapplicable for most perovskites with broken symmetry. This further highlights the advantage of studying defect dynamics in  $\text{KTaO}_3$ .
- <sup>52</sup>A recent shell model/semiempirical Hartree Fock study predicts an oxygen vacancy hopping barrier of order 0.7–0.8 eV in  $\text{KNbO}_3$ , which is similar to the systems considered herein. The saddle point atomic configuration is predicted to have a symmetry similar to the one considered in this work. See P.W.M. Jacobs, E.A. Kotomin, and R.I. Eglitis, *J. Phys.: Condens. Matter* **12**, 569 (2000).
- <sup>53</sup>W.-K. Lee, A.S. Nowick, and L.A. Boatner, *Adv. Ceram.* **23**, 387 (1987).
- <sup>54</sup>Because of the small activation energy, climbing image NEB does not improve the convergence.
- <sup>55</sup>An NMR study of this off center Li-reorientation dynamics also gives an activation energy below 0.1 eV. See J.J. van der Klink and F. Borsa, *Phys. Rev. B* **30**, 52 (1984).
- <sup>56</sup>O. Hanske-Petitpierre, Y. Yacoby, J. Mustre de Leon, E.A. Stern, and J.J. Rehr, *Phys. Rev. B* **44**, 6700 (1991).
- <sup>57</sup>S. Triebwasser, *Phys. Rev.* **101**, 993 (1956).

<sup>58</sup>J.J. van der Klink, S. Rod, and A. Châtelain, Phys. Rev. B **33**, 2084 (1986).

<sup>59</sup>Because Ca off-center displacement can be expected to be sensitive to the soft-mode frequency, which LDA does not reproduce

quantitatively, it cannot be completely ruled out (although it is highly unlikely) that Ca may in reality displace off-center in unstrained  $\text{KTaO}_3$ , even in the absence of Nb.

<sup>60</sup>Clustering has been investigated in Ref. 26 for uncharged defects.